ACS APPLIED MATERIALS & INTERFACES

Research Article

www.acsami.org

Chemical Protection of ZnO Nanorods at Ultralow pH To Form a Hierarchical $BiFeO_3$/ZnO Core–Shell Structure

Leonard Loh,[†,‡] Joe Briscoe,*[,†] and Steve Dunn[†]

[†]Materials Research Institute, School of Engineering and Materials, Queen Mary University of London, London E1 4NS, United Kingdom

[‡]School of Engineering, Nanyang Polytechnic, Singapore 569830, Singapore

Supporting Information

ABSTRACT: ZnO is an interesting material for photoactive and optoelectronic devices because of the wide range of available nanostructures and advantageous semiconducting properties. However, a significant drawback of ZnO is the low stability in high or low pH solutions. This has limited the development of ZnO core–shell materials for use in Z-scheme systems or photovoltaics, where any secondary phase is produced using chemical solution processing at low or high pH. Here, we show a simple process to produce an organic capping layer of 3-aminopropyltriethoxysilane that can successfully stabilize nanostructured ZnO for processing below pH 1. We demonstrate that this process can be used to produce a ZnO–$BiFeO_3$ (BFO) core–shell structure by a sol–gel process. Using a range of physical and analytical techniques, we show that BFO is highly crystalline and produces a conformal coating with a thickness of 2.5 nm. X-ray photoelectron spectroscopy and X-ray diffraction confirm the phase and expected chemical composition of BFO. Finally we are able to demonstrate that diodes produced using the ZnO–BFO core–shell structure have improved performance with a rectification ratio at ±3 V of 2800 because of the reduction in reverse current typically associated with surface recombination on ZnO. Our process opens a route to producing a range of hitherto prohibited ZnO core–shell structures that may have applications ranging from photovoltaic devices to core–shell photocatalysts.

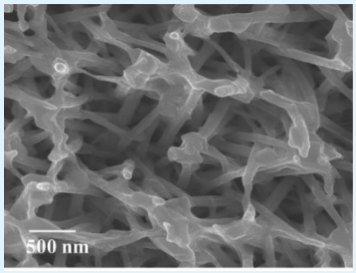

KEYWORDS: *nanostructure, chemical protection, ZnO, BFO, APTES*

INTRODUCTION

ZnO has been widely researched for a range of diverse electronic, optoelectronic, and photocatalytic applications because of its high electronic mobility (205–300 cm^2 V s^{-1}),[1] high electron diffusion coefficient (1.7×10^{-4} cm^2 s^{-1}),[2] well-positioned band structure, and ease of synthesizing as a nanostructure. ZnO has been extensively investigated as a backbone material for a range of optoelectronic devices, including solar cells, photodiodes, and light-emitting devices. In all of these areas, a key limitation has been a lack of available solution processing routes to produce heterostructures when a high or low pH is required. An example is in the area of solar cells, where the wide band gap ZnO has been enhanced using different types of sensitizers, such as dyes, quantum dots, solid-state semiconductors, or organic hole conductors, which enhance the absorption of visible light.[3] However, a significant problem has been the lack of stability of ZnO in acidic or basic conditions;[4,5] dye-sensitized ZnO solar cells have been reported to be unstable,[6,7] and unprotected ZnO cannot be used as the basis for a heterostructure, where a strong acid is required to dissolve a metal or to produce a stable solution for inorganic material growth, because it will dissolve.

Recently, there has been growing and intense interest in the use of perovskite-structured materials, such as the organometal trihalide $CH_3NH_3PbI_3$[8,9] and $CsSnI_3$[10] because they have shown significant improvements in the performance of metal-oxide-based dye-sensitized solar cells. Many polar materials that are ferroelectric share the same perovskite crystal structure, and we have for some time been focusing on using polar materials, such as piezoelectric ZnO,[11] and ferroelectric materials, such as $LiNbO_3$ and $BaTiO_3$, for solar energy conversion systems.[12,13] Interest in these polar materials stems from a variety of physical and photophysical phenomena. The inherent dipole in a ferroelectric acts to separate internal carriers and influences photochemistry,[14] and in the case of a piezoelectric material, we have shown that strain induced through sound can have an impact on carrier lifetime.[15] Additionally, the bulk photovoltaic (PV) effect of a ferroelectric stems from the band bending of the material induced because of the surface depolarization field. Ferroelectric materials, such as $BaTiO_3$,[16] $LiNbNO_3$, LSMO/SNTO,[17] $BaSnO_3$, and KBNNO,[18] show properties that are inherent and are attributed to the non-centrosymmetry of these crystals in the *c* axis.[19] In some specific instances, measurements have shown that a "greater than bandgap" voltage[16] can form in the direction of the electrical polarization, proportional to the crystal size. Our previous experience working with ferroelectric and also the multiferroic perovskite $BiFeO_3$ (BFO)[20] led an interest to develop a process to produce BFO on nanostructured ZnO to combine the functionalities of these two materials.

Received: July 31, 2014
Accepted: September 23, 2014
Published: September 23, 2014

There have previously only been a limited number of reports that show BFO deposited on ZnO, all of which have used vacuum-based techniques. Such techniques are inappropriate to produce a true homogeneous coverage of a nanostructure, because in many cases, there is a "shadowing" effect that prevents complete coverage. Additionally, vacuum techniques are not transferable to nanoparticles because there are significant processing hurdles to overcome to produce good particle coverage. The processes reported to date include the use of a $LaNiO_3$ buffer layer,[21] ZnO used as a buffer layer on $SrRuO_3/Pt(111)/TiO_2/SiO_2/Si(100)$ substrates,[22] and Pb-$(Zr_{0.52}Ti_{0.48})O_3/BiFeO_3$ (PZT−BFO) on ZnO[23] and on Si substrates.[24] None of the reports used chemical solution methods to deposit BFO on ZnO, because of the poor chemical stability of ZnO in acidic[4] and alkaline environments, such as NaOH.[25,26] We have refined a commonly used process of using a 3-aminopropyltriethoxysilane [APTES, $H_2N(CH_2)_3Si(OC_2H_5)_3$] layer to functionalize surfaces,[27] to be used as a protective layer for nanostructured ZnO against dissolution in a solution with pH less than 1. This technique could readily be transferred to nanoparticles of ZnO that are in solution as well as the high aspect ratio nanorods that we have tested in this work. As such, we present a technique that can enable a variety of low pH chemical solution deposition processes to be transferred to ZnO.

EXPERIMENTAL SECTION

ZnO Nanorod Synthesis. A total of 15 Ω sq^{-1} fluorine-doped tin oxide (FTO)-coated glass was used for transparent conductive oxide (TCO) substrates. To obtain good nucleation, 30 nm of the ZnO seed layer was deposited on the FTO substrate by magnetron sputtering using the Denton Vacuum Explorer 14 physical vapor deposition (PVD) machine with a power of 125 W, base pressure of 4×10^{-2} mTorr, and working pressure of 100 mTorr, at ambient temperature in 100% Ar atmosphere. The ZnO nanorods were synthesized by suspending the seeded substrates facedown in a solution of 25 mM zinc nitrate [$Zn(NO_3)_2 \cdot 6H_2O$] and 25 mM hexamethylenetetramine or HMT ($C_6H_{12}N_4$) in deionized (DI) water at 90 °C for 2.5 h, after which the reactants were depleted.[11] The process was repeated 6 times with fresh solutions for a total reaction time of 15 h.

APTES Coating. To prevent ZnO from dissolving in the acidic BFO sol, an APTES buffer layer was added prior to the chemical solution deposition of BFO.[28] The influence of the silanization process was tested by soaking ZnO nanorods in APTES dissolved in toluene at concentrations ranging from 2 to 6% by volume at 60 °C. Soaking times of 0.5−15 h were investigated, and the final sample was then rinsed clean with toluene. The samples were then annealed at 90 °C for 1 h to cure the APTES coating prior to BFO coating.

BFO Sol−Gel Coating. Kapton tape was used to cover an edge of the samples to prevent BFO coating. The BFO coating was deposited by spin coating at 5000 rpm using a sol made from bismuth nitrate pentahydrate [$Bi(NO_3)_3 \cdot 5H_2O$] and iron nitrate nonahydrate [$Fe(NO_3)_3 \cdot 9H_2O$] mixed in 2-methoxyethanol ($CH_3OCH_2CH_2OH$). A total of 20% by volume of acetic anhydride [$(CH_3CO)_2O$] and 2% by volume of ethanolamine were added to act as a dehydrating agent and adjust the viscosity, respectively. The samples were heated at 100 °C for 1 min to stabilize the film, followed by pre-annealing at 350 °C for 3 min to degrade APTES.[29] Final annealing temperatures of 400−650 °C for 2 h in air were investigated for BFO on ZnO samples.[30] The nature of the bonding of the APTES layer to the ZnO surface was investigated using PerkinElmer spectrum 400 Fourier transform infrared (FTIR) spectroscopy in the range of 650−4000 cm^{-1}.

Material Characterization. A Jeol JSM 6701F field emission scanning electron microscope (FESEM) was used to image the morphology, cross-section, and surfaces of the films as well as for energy-dispersive X-ray analysis. X-ray diffraction (XRD) peaks were measured using a Panalytical X'pert Pro X-ray diffractometer using Cu Kα. X-ray photoelectron spectroscopy (XPS) analysis of the samples was carried out using Thermo Scientific Theta Probe XPS. Monochromatic Al Kα X-ray ($h\nu$ = 1486.6 eV) was employed for analysis, with an incident angle of 30° with respect to the surface normal. Photoelectrons were collected at a takeoff angle of 50° with respect to the surface normal. The analysis area was approximately 400 μm in diameter. Charge compensation was performed by means of a low energy electron flooding, and further correction was made based on adventitious C 1s at 285.0 eV. The error of binding energy was estimated to be within ±0.2 eV.

Device Fabrication and Characterization. Surlyn film was used as a barrier layer, with holes of 6 mm diameter for the active areas. Diodes were spray-coated with CuSCN from a prepared solution of 0.2 M CuSCN in dipropyl sulfide using an Iwata airbrush system while heating at 90 °C on a hot plate.[31] Au counter electrodes (150 nm thick) were sputtered using the Denton Vacuum Explorer 14 thermal evaporator using a power of 125 W, base pressure of 4×10^{-2} mTorr, and working pressure of 100 mTorr, at ambient temperature in 100% Ar atmosphere. Ferroelectric measurements were conducted on a 520 nm thick BFO film using a ferroelectric tester, with frequencies ranging from 1 to 100 Hz, and input triangular waveforms from the Agilent 33120A function generator, with a TREK 610E amplifier and a Stanford Research Systems SR570 low-noise current amplifier. The $J-V$ characteristics were tested with the Keithley 2400 source meter, with input voltage scanning from −5 to 5 V under dark conditions at room temperature.

RESULTS AND ANALYSIS

The ZnO nanorods had an average length of 2.5 μm and diameter of 130 nm (see Figure S1 of the Supporting Information). The nanorods were close to perpendicular to the substrate with slight tilt variations because of inconsistencies in the crystallinity of the seed layer as well as roughness of the FTO. XRD of ZnO showed a hexagonal wurtzite structure with significantly strong polar (0002) planes with smaller crystallographic nonpolar planes because of slight variations in the orientation of the rods.

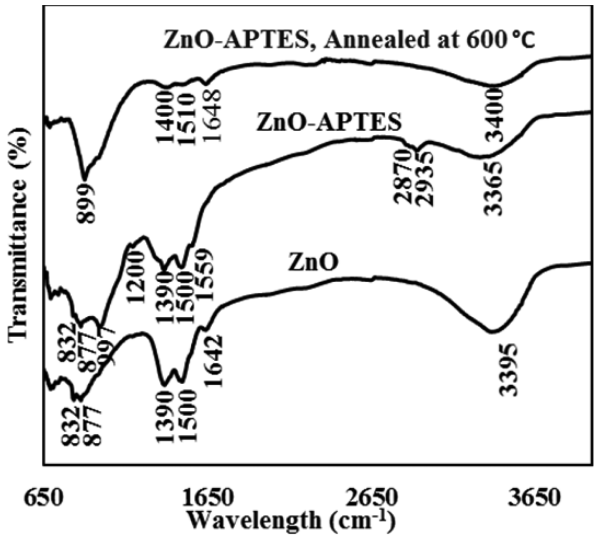

Figure 1. FTIR spectra of ZnO and ZnO coated with APTES coating.

The ZnO surface contains hydroxyl groups either chemisorbed or physiorbed, as shown in Figure 1, associated with a stretching frequency around 3400 cm^{-1} in the FTIR spectra. Characteristic peaks are at 832 and 877 cm^{-1} for Zn−O stretching and 1390 cm^{-1} for O−H bending vibration, with a small peak at 1642 cm^{-1} for C═O stretching of the carbonyl

dx.doi.org/10.1021/am505019p | ACS Appl. Mater. Interfaces 2015, 7, 152−157

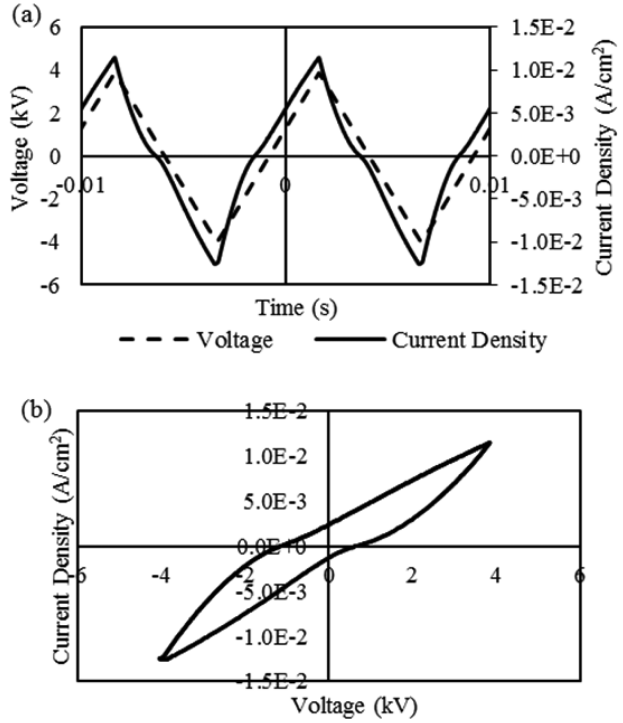

Figure 2. Ferroelectric measurements of the 520 nm thick BFO film with a 4 V charging amplitude and 100 Hz frequency: (a) voltage and current output in the time domain and (b) voltage–current density curves for the devices.

group from residual precursor products, as shown previously.[29] It is known that hydrolysis of APTES forming silanol (SiOH) occurs mainly on the surface of ZnO.[32] Si–OH was detected in the reduction of the broad peak around 3400 cm^{-1} in the FTIR spectra. Condensation occurs between two surface-bound APTES molecules to form siloxane (Si–O–Si), detected with the asymmetric stretching vibration around 997 cm^{-1}. A number of further peaks at 2935 and 2870 cm^{-1} are all related to the binding of APTES with ZnO. (see Figure S2 of the Supporting Information) This bonding of APTES to ZnO is in agreement with FTIR data in previous reports.[29] We also show in Figure 1 that, after the 600 °C annealing of BFO, the peaks associated with the APTES bonding have disappeared.

A BFO film was spin-coated directly onto FTO and annealed at 400, 500, 600, and 650 °C. At 400 °C, no crystalline BFO was detected (see Figure S3 of the Supporting Information). Rhombohedral *R*3*c* crystalline BFO was detected at 500 °C. At 650 °C, the most highly crystalline BFO was formed with no secondary phases. However, the FTO-coated glass substrate softened at 650 °C, resulting in occasions where the glass melted in patches on the ZnO–BFO nanostructures. We therefore selected 600 °C as the processing temperature for further investigation.

Ferroelectric measurements were conducted on the BFO film with various applied voltages and frequencies. The current density–voltage plot in Figure 2 with an applied voltage of 4 V shows contribution from the dielectric permittivity and electrical conductivity. The steep slant of the loop indicates that the electrical conductivity is the major contribution. The current density–time domain plot shows no significant change in the current waveform with respect to the triangular voltage

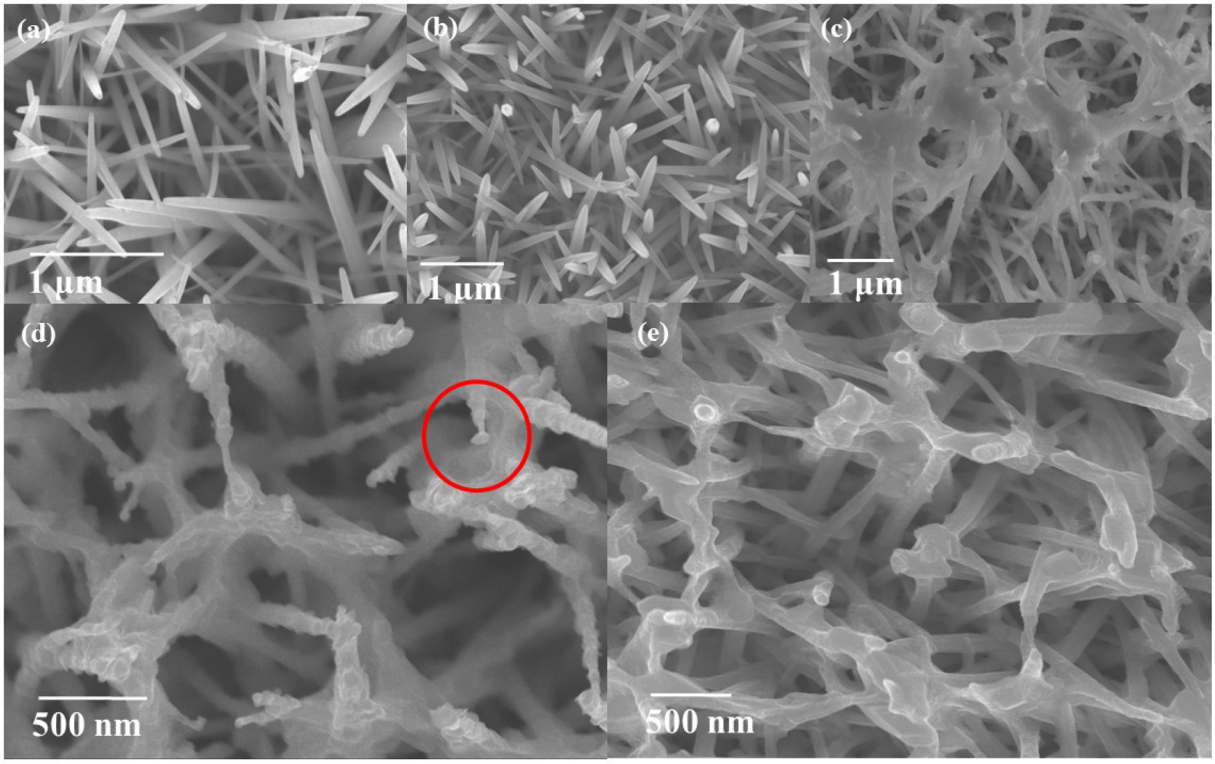

Figure 3. Scanning electron microscopy (SEM) images of APTES coating on ZnO nanorods. APTES concentration at (a) 2%, (b) 4%, and (c) 6% APTES volume in toluene soaked for 30 min. BFO sol spin-coated with 0.3 M BFO sol on (d) 2% APTES coating, showing some degradation of ZnO nanorods, and (e) 4% APTES coating, showing effective protection of ZnO nanorods.

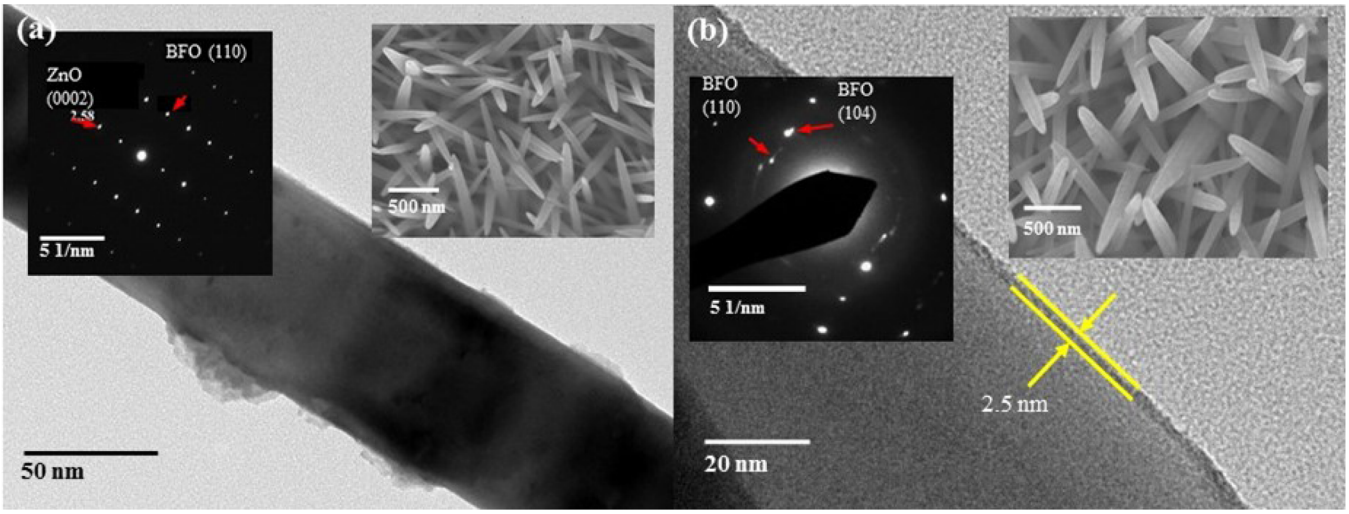

Figure 4. Images of BFO coating on ZnO nanorods: (a) transmission electron microscopy (TEM) of island-like coated BFO and (b) TEM of conformally coated BFO. The insets show corresponding SAED and SEM images.

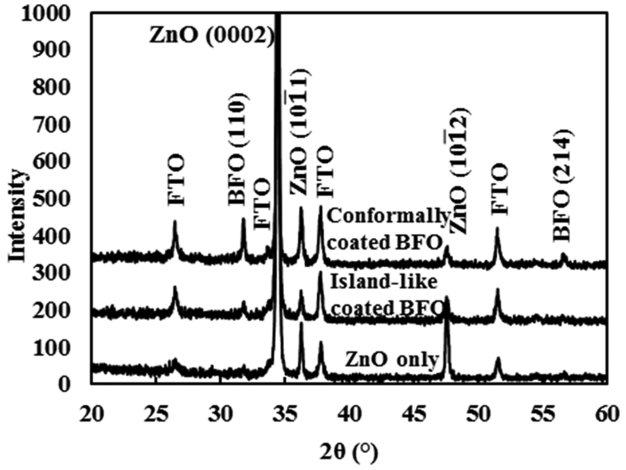

Figure 5. XRD patterns of ZnO on FTO with varying BFO thicknesses.

input, even though slight phase shifting of the current appears to occur. This indicates that the BFO domains start to switch, but because of losses from the valence fluctuations of Fe^{3+} to Fe^{2+}, no eventual switching occurs. No hysteresis loop was also obtained in the polarization−voltage plot. Several reports indicate that BFO synthesized from sol−gel techniques exhibits poor or no ferroelectric properties due to the high oxygen vacancies existing in BFO.[33]

Three concentrations of APTES were investigated to coat the ZnO: 2, 4 and 6% by volume in toluene. Figure 3 shows that, at an APTES concentration of 2%, the tips of the nanorods appear thinner with some etching, indicating that APTES did not offer complete protection. At 4% APTES concentration, the BFO-coated nanorods had clearly defined structures, indicating full protection. Increasing the APTES concentration to 6% increased the potential of excessive APTES coating (Figure 3c).

Two concentrations of the BFO sol were investigated: 0.075 and 0.15 M. As shown in Figure 4, the 0.075 M concentration gave a series of BFO islands on the ZnO surface and the higher

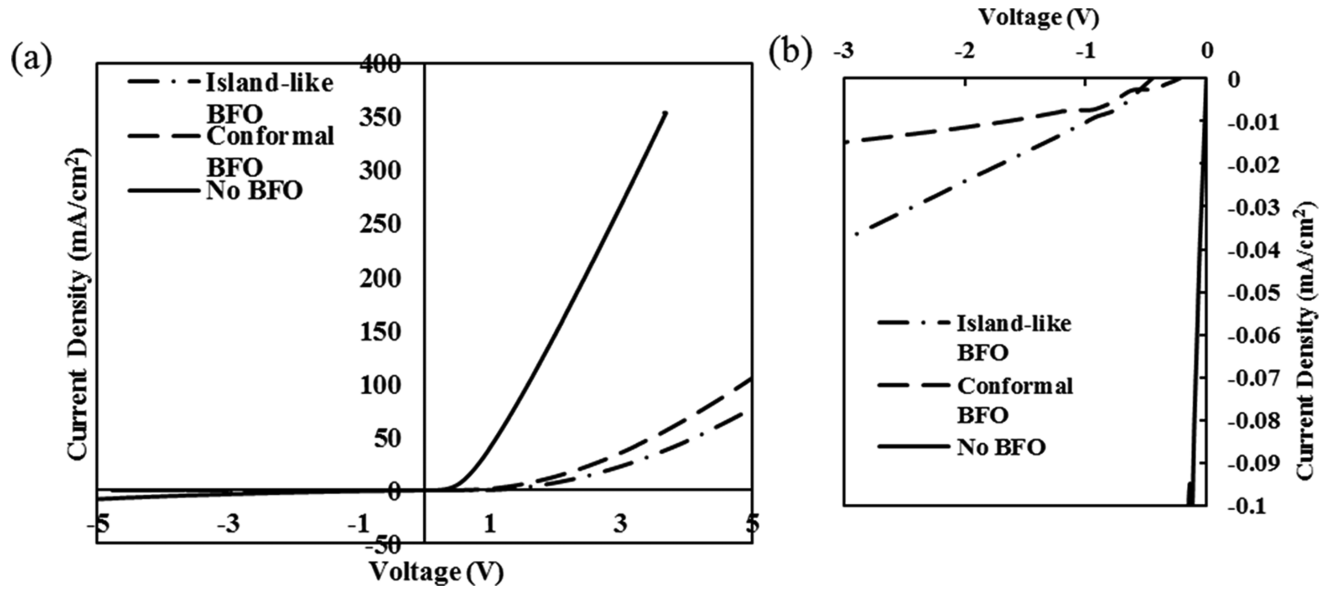

Figure 6. *J*−*V* characteristics of ZnO and ZnO−BFO devices under dark current conditions (a) from −5 to +5 V and (b) under negative bias.

dx.doi.org/10.1021/am505019p | ACS Appl. Mater. Interfaces 2015, 7, 152−157

0.15 M concentration gave a conformal coating. The measured pH of the BFO sol was 0.8 for 0.15 M and 2.75 for 0.075 M. Full conformal coverage of the ZnO nanorods with the 0.15 M BFO sol concentration gave an average thickness of BFO of 2.5 nm (Figure 4b). The XRD (Figure 5) shows that crystalline BFO has been deposited on ZnO nanorods. To further confirm the presence of crystalline BFO, the selected area electron diffraction (SAED) pattern determined that (104) and (110) crystalline planes of BFO were present, as seen in Figure 4. The formation of crystalline BFO indicates that the nucleation of BFO was achieved on ZnO as a result of the close lattice match because the BFO planes with spacing closest to the ZnO (0002) plane were dominant. Figure S4 of the Supporting Information shows the XPS analysis of a single coated BFO film on FTO, spin-coated using 0.3 M BFO, which is typical of the XPS expected for BFO.[21,34]

A series of diodes using the ZnO−BFO architectures were produced to determine the influence on carrier transport. In the absence of BFO, the diode shows behavior as would be expected from previously reported work.[31,35] The $J-V$ plot of representative devices in Figure 6 shows that the BFO-coated devices show a consistent turn on voltage around 0.25 V. The rectification ratios for the BFO-coated devices at ±3 V were ca. 900 for island-like coverage and ca. 2800 for conformally coated BFO devices. This compares to ca. 70 for uncoated ZnO devices. The leakage current at −3 V for the ZnO diode was significantly higher, measured at 3.5 mA, while the BFO devices had a lower leakage current of 0.04 mA for island-like BFO and 0.015 mA for conformally coated BFO devices.

The large offset between the conduction and valence bands of ZnO and CuSCN (see Figure S5 of the Supporting Information) reduces the probability of conventional current transport at low bias. Therefore, recombination currents at low bias and defect-assisted tunneling at higher bias are the main transport mechanisms for a ZnO/CuSCN device.[36] The addition of a BFO layer to ZnO creates a barrier to carrier tunneling from ZnO to CuSCN and, therefore, reduces carrier recombination and also slightly reduces the magnitude of the forward current.

If we consider the forward bias of the devices with BFO, we can see only a small variation in behavior between conformal and island coating. This variation is within the expected variability of device-to-device production based on the large number of devices that we have tested. However, investigating the negative bias (Figure 6b) and relating this to the rectification behavior, we can see a significant influence of the conformal coating of the BFO. In contrast to the small change to the forward bias current upon the addition of BFO, the reverse bias current is significantly reduced. This is due to the reduction in recombination of carriers and the blocking effect of the BFO layer.[37]

Tests on ZnO nanostructures that had been processed with APTES and had no BFO added before being made into diodes showed no change in behavior over a standard ZnO−CuSCN diode, indicating that the performance changes are indeed from the presence of the BFO.

CONCLUSION

This paper reports a technique used to deposit BFO on ZnO using chemical solution techniques by adding a buffer layer of APTES on ZnO, which acts to protect ZnO during a chemically aggressive process. Improved diode performance was measured with BFO-coated devices, showing higher switch on voltages and an improved rectification of ca. 2800 at ±3 V. The process reported herein opens the opportunity to produce a range of ZnO nanostructures that are hierarchical or core−shell using previously restricted techniques of high or low pH chemical solution processing.

ASSOCIATED CONTENT

Supporting Information

SEM/XRD of ZnO and BFO (Figures S1 and S3), bonding reaction between APTES and ZnO (Figure S2), XPS of BFO (Figure S4), and schematic energy band alignment for the diode structure (Figure S5). This material is available free of charge via the Internet at http://pubs.acs.org.

AUTHOR INFORMATION

Corresponding Author

*E-mail: j.briscoe@qmul.ac.uk.

Notes

The authors declare no competing financial interest.

ACKNOWLEDGMENTS

Funding from the Leverhulme Trust is acknowledged. We would also like to acknowledge the help of Haixue Yan in producing the ferroelectric hysteresis measurements.

REFERENCES

(1) Zhang, Q. F.; Dandeneau, C. S.; Zhou, X. Y.; Cao, G. Z. ZnO nanostructures for dye-sensitized solar cells. *Adv. Mater.* **2009**, *21*, 4087−4108.

(2) Zhang, Q. F.; Cao, G. Z. Nanostructured photoelectrodes for dye-sensitized solar cells. *Nano Today* **2011**, *6*, 91−109.

(3) Loh, L.; Dunn, S. Progress in ZnO-based nanostructured ceramics in solar cell applications. *J. Nanosci. Nanotechnol.* **2012**, *12*, 8215−8230.

(4) Cetinorgu, E.; Goldsmith, S. Chemical and thermal stability of the characteristics of filtered vacuum arc deposited ZnO, SnO_2 and zinc stannate thin films. *J. Phys. D: Appl. Phys.* **2007**, *40*, 5220−5226.

(5) Olvera, M. D. L.; Maldonado, A.; Asomoza, R.; Melendez-Lira, M. Chemical stability of doped ZnO thin films. *J. Mater. Sci.: Mater. Electron.* **2000**, *11*, 1−5.

(6) Anta, J. A.; Guillen, E.; Tena-Zaera, R. ZnO-based dye-sensitized solar cells. *J. Phys. Chem. C* **2012**, *116*, 11413−11425.

(7) Hoye, R. L. Z.; Musselman, K. P.; MacManus-Driscoll, J. L. Research update: Doping ZnO and TiO_2 for solar cells. *APL Mater.* **2013**, *1*, 060701.

(8) Bi, D.; Boschloo, G.; Schwarzmuller, S.; Yang, L.; Johansson, E. M. J.; Hagfeldt, A. Efficient and stable $CH_3NH_3PbI_3$-sensitized ZnO nanorod array solid-state solar cells. *Nanoscale* **2013**, *5*, 11686−11691.

(9) Kumar, M. H.; Yantara, N.; Dharani, S.; Graetzel, M.; Mhaisalkar, S.; Boix, P. P.; Mathews, N. Flexible, low-temperature, solution processed ZnO-based perovskite solid state solar cells. *Chem. Commun.* **2013**, *49*, 11089−11091.

(10) Chung, I.; Lee, B.; He, J. Q.; Chang, R. P. H.; Kanatzidis, M. G. All-solid-state dye-sensitized solar cells with high efficiency. *Nature* **2012**, *485*, 486−490.

(11) Briscoe, J.; Gallardo, D. E.; Hatch, S.; Lesnyak, V.; Gaponik, N.; Dunn, S. Enhanced quantum dot deposition on ZnO nanorods for photovoltaics through layer-by-layer processing. *J. Mater. Chem.* **2011**, *21*, 2517−2523.

(12) Stock, M.; Dunn, S. $LiNbO_3$—A new material for artificial photosynthesis. *IEEE Trans. Ultrason. Eng.* **2011**, *58*, 1988−1993.

(13) Cui, Y.; Briscoe, J.; Dunn, S. Effect of ferroelectricity on solar-light-driven photocatalytic activity of $BaTiO_3$—Influence on the carrier separation and stern layer formation. *Chem. Mater.* **2013**, *25*, 4215−4223.

(14) Dunn, S.; Jones, P. M.; Gallardo, D. E. Photochemical growth of silver nanoparticles on c^- and c^+ domains on lead zirconate titanate thin films. *J. Am. Chem. Soc.* **2007**, *129*, 8724−8728.
(15) Briscoe, J.; Stewart, M.; Vopson, M.; Cain, M.; Weaver, P. M.; Dunn, S. Nanostructured p-n junctions for kinetic-to-electrical energy conversion. *Adv. Energy Mater.* **2012**, *2*, 1261−1268.
(16) Brody, P. S.; Crowne, F. Mechanism for high-voltage photovoltaic effect in ceramic ferroelectrics. *J. Electron. Mater.* **1975**, *4*, 955−971.
(17) He, X.; Jin, K.; Ge, C.; Wang, C.; Lu, H.; Yang, G. The mechanism of the maximum photovoltage in perovskite oxide heterostructures with the critical thickness. *EPL* **2013**, *102*, 37007.
(18) Grinberg, I.; West, D. V.; Torres, M.; Gou, G.; Stein, D. M.; Wu, L.; Chen, G.; Gallo, E. M.; Akbashev, A. R.; Davies, P. K.; Spanier, J. E.; Rappe, A. M. Perovskite oxides for visible-light-absorbing ferroelectric and photovoltaic materials. *Nature* **2013**, *503*, 509−512.
(19) Glass, A. M.; Linde, D. V. D.; Negran, T. High-voltage bulk photovoltaic effect and the photorefractive process in $LiNBO_3$. *J. Appl. Phys. Lett.* **1974**, *25*, 233−235.
(20) Hengky, C.; Moya, X.; Mathur, N. D.; Dunn, S. Evidence of high rate visible light photochemical decolourisation of rhodamine B with $BiFeO_3$ nanoparticles associated with $BiFeO_3$ photocorrosion. *RSC Adv.* **2012**, *2*, 11843−11849.
(21) Chiu, K.-C.; Yang, T.-H.; Wu, J.-M. Prominent electric properties of $BiFeO_3$ shells sputtered on ZnO-nanorod cores with $LaNiO_3$ buffer layers. *Nanotechnology* **2013**, *24*, 225602.
(22) Wu, J. G.; Wang, J. Diodelike and resistive hysteresis behavior of heterolayered $BiFeO_3$/ZnO ferroelectric thin films. *J. Appl. Phys.* **2010**, *108*, 94107.
(23) Dutta, S.; Pandey, A.; Yadav, I.; Thakur, O. P.; Laishram, R.; Pal, R.; Chatterjee, R. Improved electrical properties of $PbZrTiO_3$/$BiFeO_3$ multilayers with ZnO buffer layer. *J. Appl. Phys.* **2012**, *112*, 084101.
(24) Chen, S. W.; Lee, C. C.; Chen, M. T.; Wu, J. M. Synthesis of $BiFeO_3$/ZnO core−shell hetero-structures using ZnO nanorod positive templates. *Nanotechnology* **2011**, *22*, 115605.
(25) Zhou, J.; Xu, N. S.; Wang, Z. L. Dissolving behavior and stability of ZnO wires in biofluids: A study on biodegradability and biocompatibility of ZnO nanostructures. *Adv. Mater.* **2006**, *18*, 2432−2435.
(26) Yang, Y.; Kim, D. S.; Qin, Y.; Berger, A.; Scholz, R.; Kim, H.; Knez, M.; Gosele, U. Unexpected long-term instability of ZnO nanowires "protected" by a TiO_2 shell. *J. Am. Chem. Soc.* **2009**, *131*, 13920−13921.
(27) Yakimova, R.; Steinhoff, G.; Petoral, R. M., Jr.; Vahlberg, C.; Khranovskyy, V.; Yazdi, G. R.; Uvdal, K.; Spetz, A. L. Novel material concepts of transducers for chemical and biosensors. *Biosens. Bioelectron.* **2007**, *22*, 2780−2785.
(28) Ogata, K.; Dobashi, H.; Koike, K.; Sasa, S.; Inoue, M.; Yano, M. Improvement of chemical stability of aqueous solution grown ZnO nanorods by aminosilane modification. *Phys. Status Solidi C* **2010**, *7*, 1562−1564.
(29) Mitra, S.; Chandra, S.; Laha, D.; Patra, P.; Debnath, N.; Pramanik, A.; Pramanik, P.; Goswami, A. Unique chemical grafting of carbon nanoparticle on fabricated ZnO nanorod: Antibacterial and bioimaging property. *Mater. Res. Bull.* **2012**, *47*, 586−594.
(30) Liu, H. R.; Liu, Z. L.; Liu, Q.; Yao, K. L. Ferroelectric properties of $BiFeO_3$ films grown by sol−gel process. *Thin Solid Films* **2006**, *500*, 105−109.
(31) Hatch, S. M.; Briscoe, J.; Dunn, S. Improved CuSCN−ZnO diode performance with spray deposited CuSCN. *Thin Solid Films* **2013**, *531*, 404−407.
(32) Grasset, F.; Saito, N.; Li, D.; Park, D.; Sakaguchi, I.; Ohashi, N.; Haneda, H.; Roisnel, T.; Mornet, S.; Duguet, E. Surface modification of zinc oxide nanoparticles by aminopropyltriethoxysilane. *J. Alloys Compd.* **2003**, *360*, 298−311.
(33) Kumar, M. M.; Palkar, V. R.; Srinivas, K.; Suryanarayana, S. V. Large magnetization and weak polarization in sol−gel derived $BiFeO_3$ ceramics. *Appl. Phys. Lett.* **2000**, *76*, 2764−2766.
(34) Liu, W.; Tan, G.; Xue, X.; Dong, G.; Ren, H. Structure transition and enhanced ferroelectric properties of (Mn, Cr) Co-doped $BiFeO_3$ thin films. *J. Mater. Sci.: Mater. Electron.* **2013**, *24*, 4827−4832.
(35) Hatch, S. M.; Briscoe, J.; Dunn, S. A self-powered ZnO-nanorod/CuSCN UV photodetector exhibiting rapid response. *Adv. Mater.* **2013**, *25*, 867−871.
(36) Xiong, C.; Yao, R. H.; Wan, W. J.; Xu, J. X. Fabrication and electrical characterization of ZnO rod arrays/CuSCN heterojunctions. *Optik* **2014**, *125*, 785−788.
(37) Loh, L.; Briscoe, J.; Dunn, S. Enhanced performance with bismuth ferrite perovskite in ZnO nanorod solid state solar cell. *Nanoscale* **2014**, *6*, 7072−7078.